**PASJ:** Publ. Astron. Soc. Japan **60**, S333–S342, 2008 February 20
© 2008. Astronomical Society of Japan.

# Suzaku Observations of AWM 7 Cluster of Galaxies: Temperatures, Abundances, and Bulk Motions

Kosuke SATO,[1,2] Kyoko MATSUSHITA,[1] Yoshitaka ISHISAKI,[2] Noriko Y. YAMASAKI,[3] Manabu ISHIDA,[3] Shin SASAKI,[2] and Takaya OHASHI[2]

[1] *Department of Physics, Tokyo University of Science, 1-3 Kagurazaka, Shinjuku-ku, Tokyo 162-8601*
*ksato@rs.kagu.tus.ac.jp*

[2] *Department of Physics, Tokyo Metropolitan University, 1-1 Minami-Osawa, Hachioji, Tokyo 192-0397*

[3] *Institute of Space and Astronautical Science (ISAS), Japan Aerospace Exploration Agency, 3-1-1 Yoshinodai, Sagamihara, Kanagawa 229-8510*

(Received 2007 June 27; accepted 2007 July 23)

**Abstract**

We carried out 3 observations of the cluster of galaxies AWM 7, for the central region and 20′-east and 20′-west offset regions, with Suzaku. Temperature and abundance profiles were measured out to $27' \simeq 570\, h_{70}^{-1}$ kpc, which corresponded to $\sim 0.35\, r_{180}$. The temperature of the intra-cluster medium (ICM) slightly decreased from 3.8 keV at the center to 3.4 keV in the $\sim 0.35\, r_{180}$ region, indicating a flatter profile than those in other nearby clusters. The abundance ratio of Si to Fe was almost constant in our observations, while the Mg-to-Fe ratio increased with radius from the cluster center. The O to Fe ratio in the west region showed an increase with radius, while that in the east region was almost flat, though the errors were relatively large. These features suggest that the enrichment process is significantly different between products of type II supernovae (O and Mg) and those by type Ia supernovae (Si and Fe). We also examined the positional shift of the central energy of a He-like Fe-K$\alpha$ line, in search of possible rotation of the ICM. The 90% upper limit for the line-of-sight velocity difference was derived to be $\Delta v \lesssim 2000\,\mathrm{km\,s^{-1}}$, suggesting that the ellipticity of AWM 7 is rather caused by a recent directional infall of gas along the large-scale filament.

**Key words:** galaxies: clusters: individual (AWM 7) — X-rays: galaxies: clusters

## 1. Introduction

The mass profile of a cluster, which is a useful parameter for constraining the cosmology, is determined through X-ray measurements of the temperature and density structure of the ICM under the assumption of hydrostatic equilibrium of the ICM. Recent observations have shown spatially resolved spectra of clusters with good spatial and spectral resolution, and have revealed the temperature and abundance profiles for many systems. Markevitch et al. (1998) analyzed the spectra of 30 nearby clusters with ASCA and ROSAT, and reported that most of them showed a similar temperature decline at large radii. However, White (2000) studied a sample of 106 clusters observed with ASCA, and found that 90% of the temperature profiles were consistent with being isothermal. Piffaretti et al. (2005) showed temperature profiles of 13 nearby cooling flow clusters with XMM-Newton; the temperature decreased by $\sim 30\%$ between 0.1 and 0.5 $r_{180}$ using the virial radius $r_{180}$, in good agreement with the results of Markevitch et al. (1998). Recent measurements of 13 nearby relaxed clusters with Chandra by Vikhlinin et al. (2005) also indicated that the temperature reached a peak at $r \sim 0.15\, r_{180}$, and then declined to about half of its peak value at $r \sim 0.5\, r_{180}$.

Chandra and XMM-Newton observations also allowed detailed studies of metal abundance in the ICM. However, these observations showed metal-abundance profiles from O to Fe only for the central region of bright clusters, or groups of galaxies dominated by cD galaxies in a reliable manner (Finoguenov et al. 2002; Fukazawa et al. 2004; Matsushita et al. 2003; Tamura et al. 2004; Matsushita et al. 2007). The abundances of O and Mg in the cluster outer regions are still poorly determined, because these satellites show a relatively high intrinsic background. Because of the low and stable background and the good resolving power for emission lines below 1 keV, the Suzaku XIS instrument (Koyama et al. 2007) can precisely measure not only the temperature close to the virial radius of the cluster, but also the abundances of O to Fe to outer regions (Sato et al. 2007a), compared with the past observations.

Clusters are also thought to grow into larger systems through complex interactions between smaller systems. It is expected that evidence of merger events can be found as non-Gaussian velocity distributions of galaxies, temperature and density inhomogeneities in the ICM, and bulk motions of the ICM. Furusho et al. (2003) found the inhomogeneous ICM to have blob-like structure in the central region of AWM 7 with Chandra. Hayakawa et al. (2006) also found inhomogeneous structure to have the high metallicity blob in the central region of Abell 1060 with Chandra and XMM-Newton. Though Dupke and Bregman (2006) showed a large velocity gradient of $2400 \pm 1000\,\mathrm{km\,s^{-1}}$ over a spatial scale of 100 kpc in the Centaurus cluster with Chandra, reconfirming their previous ASCA measurement (Dupke & Bregman 2001), Ota et al. (2007) gave a negative result of $\Delta v < 1400\,\mathrm{km\,s^{-1}}$, based on a measurement with Suzaku.

AWM 7 is a nearby cluster of galaxies ($z = 0.01724$)

Downloaded from https://academic.oup.com/pasj/article/60/sp1/S333/1461691 by guest on 16 August 2022

**Table 1.** Suzaku observation of AWM 7.

| Target name | Sequence number | Date | Exposure time | (RA, Dec)* in J2000.0 | After screening |
|---|---|---|---|---|---|
| AWM 7 center | 801035010 | 2006-Aug-7 | 19.0 ks | ($2^h54^m32^s.0$, $+41°35'15''$) | 18.9 ks |
| AWM 7 east | 801036010 | 2006-Aug-5 | 38.5 ks | ($2^h56^m08^s.4$, $+41°35'18''$) | 38.3 ks |
| AWM 7 west | 801037010 | 2006-Aug-6 | 39.8 ks | ($2^h52^m55^s.8$, $+41°35'16''$) | 39.7 ks |

* Average pointing direction of the XIS, written in the RA_NOM and DEC_NOM keywords of the event FITS files.

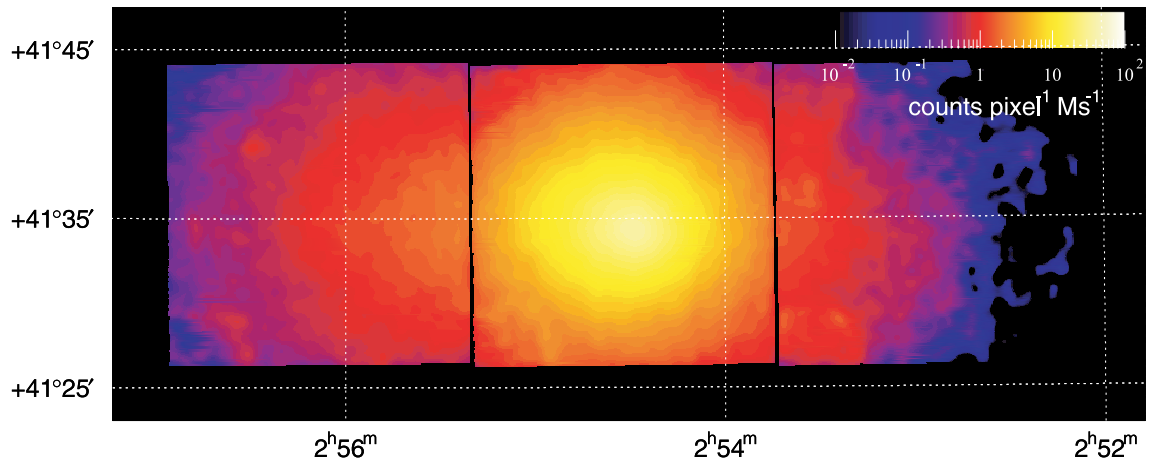


**Fig. 1.** Combined XIS image of central and offset observations in the 0.5–7.0 keV energy range. The observed XIS 0–3 images were added on the sky coordinates after removing each calibration source region, and smoothed with $\sigma = 16$ pixel $\simeq 17''$ Gaussian. Estimated components of extragalactic X-ray background (CXB) and instrumental background (NXB) were subtracted, and the exposure was corrected, though vignetting was not corrected.

characterized by a smooth distribution of ICM, and has a cD galaxy, NGC 1129, at the center. In the central region within $2'$, Chandra observations showed that the temperature gradually dropped from 4 to 2 keV toward the cluster center, and the metal abundance rose steeply to a peak of 1.5 solar (Furusho et al. 2003). Ezawa et al. (1997) also indicated a large-scale abundance gradient of $\sim 40\%$ from center to the $r \sim 500$ kpc region with ASCA. Hayakawa (2006) detected a temperature drop of $\sim 10\%$ from the central region to $r \sim 13'$ with XMM-Newton, while it had previously been considered to be flat, based on ASCA observations (Furusho et al. 2001; Ezawa et al. 1997).

This paper reports on results from Suzaku observations of AWM 7 out to $27' \simeq 570\, h_{70}^{-1}$ kpc, corresponding to $\sim 0.35\, r_{180}$. We use $H_0 = 70\,\mathrm{km\,s^{-1}\ Mpc^{-1}}$, $\Omega_\Lambda = 1 - \Omega_\mathrm{M} = 0.73$ in this paper. At a redshift of $z = 0.01724$, $1'$ corresponds to 21 kpc, and the virial radius, $r_{180} = 1.95\, h_{100}^{-1} \sqrt{k\langle T\rangle/10\,\mathrm{keV}}$ Mpc (Markevitch et al. 1998), is 1.65 Mpc ($79'$) for an average temperature of $k\langle T\rangle = 3.5$ keV. Throughout this paper we adopt the Galactic hydrogen column density of $N_\mathrm{H} = 9.83 \times 10^{20}\,\mathrm{cm^{-2}}$ (Dickey & Lockman 1990) in the direction of AWM 7. Unless noted otherwise, the solar abundance table is given by Anders and Grevesse (1989), and the errors are in the 90% confidence region for a single interesting parameter.

## 2. Suzaku Observations and Data Reduction

### 2.1. *Observations*

Suzaku carried out three pointing observations for AWM 7 in 2006 August (PI: T. Ohashi), for the central region and $20'$-east and $20'$-west offset regions with exposures of 19.0, 38.5, and 39.8 ks, respectively. The observation log is given in table 1, and the combined X-ray Imaging Spectrometer (XIS: Koyama et al. 2007) image in 0.5–7 keV range is shown in figure 1. We consider only the XIS data in this paper. The XIS instrument consists of four sets of X-ray CCD (XIS 0, 1, 2, and 3). XIS 1 is a back-illuminated (BI) sensor, while XIS 0, 2, and 3 are front-illuminated (FI). The XIS was operated in the Normal clocking mode (8 s exposure per frame), with the standard $5 \times 5$ or $3 \times 3$ editing mode.

It is known that the optical blocking filters (OBF) of the XIS have gradually been contaminated by outgassing from the satellite. The thickness of the contaminant is different among the sensors, and is also dependent on the location on the CCD chips. The estimated column densities (C/O = 6 in number ratio is assumed) during the observation at the center of the CCD are given in table 2.[1] We included these effects in a calculation of the the Ancillary Response File (ARF) by the "xissimarfgen" Ftools task of 2006-10-26 version (Ishisaki et al. 2007). Since the energy resolution also slowly degraded after the launch, due to radiation damage, this effect was included in the Redistribution Matrix File (RMF) by the "xisrmfgen" Ftools task of the 2006-10-26 version.

[1] Calibration database file of `ae_xiN_contami_20061024.fits` was used for the estimation of the XIS contamination ($N = 0, 1, 2, 3$ indicates the XIS sensor).

Downloaded from https://academic.oup.com/pasj/article/60/sp1/S333/1461691 by guest on 16 August 2022

**Table 2.** Estimated column density of the contaminant for each sensor.*

| | XIS 0 | XIS 1 | XIS 2 | XIS 3 |
|---|---|---|---|---|
| Carbon ..... | 2.53 | 3.97 | 3.83 | 5.79 |
| Oxygen ..... | 0.422 | 0.662 | 0.639 | 0.964 |

* At the center of CCD, in units of $10^{18}$ cm$^{-2}$.

### 2.2. Data Reduction

We used version 1.2 processing data (Mitsuda et al. 2007), and the analysis was performed with HEAsoft version 6.1.1 and XSPEC 11.3.2t. The analysis method was almost the same as that of Sato et al. (2007a). However, because this observations was not supported by the Good-Time Intervals (GTI) given for excluding the telemetry saturation by the XIS team, we could not execute the process. The light curve of each sensor in the 0.3–10 keV range with a 16 s time bin was also examined so as to reject periods of an anomalous event rate greater or less than $\pm 3\,\sigma$ around the mean. After the above screenings, the remaining exposures of the observations were almost unchanged as shown in table 1. The exposures after screening were not so different from those before screening in table 1, which show that the non-X-ray background (NXB) was almost stable during both observations. Event screening with cut-off rigidity (COR) was not performed in our data.

In order to subtract the NXB and the extra-galactic cosmic X-ray background (CXB), we used a dark Earth database of 770 ks exposure, provided by the XIS team for the NXB, and employed the CXB spectrum given by Kushino et al. (2002). These analysis methods were also the same as in Sato et al. (2007a).

### 2.3. Generation of ARFs

A precise surface brightness profile of AWM 7 was needed to generate the Suzaku ARF, and we used the XMM-Newton image, which had much better spatial resolution than Suzaku. For this XMM-Newton data, we used MOS data (32 ks), and followed the data reduction by Hayakawa (2006). We used blank-sky data as the background (Read & Ponman 2003), and eliminated point sources in the ICM. Figure 2 shows a radial profile of AWM 7 with XMM-Newton in the 0.8–3 keV range, fitted with a double-$\beta$ model. The origin of the profile is placed at (RA, Dec) = ($2^{\rm h}54^{\rm m}27\overset{\rm s}{.}5$, $-41^\circ34'46''$) in J2000.0. The best-fit parameters are summarized in table 3. Though the fit is not acceptable, the temperature and abundance in the spectral fits had little influence on the ARF. We then generated two different ARFs for the spectrum of each region, $A^{\rm U}$ and $A^{\rm B}$, which respectively assumed uniform sky emission and $\sim 1^\circ \times 1^\circ$ size of the double-$\beta$ surface brightness profile obtained with the XMM-Newton data (table 3). We did not use the raw XMM-Newton image, but the smoothed surface brightness profile to generate the ARFs, because the raw XMM image had a gap between the CCD chips, and AWM 7 was characterized by a smooth and symmetric ICM distribution.

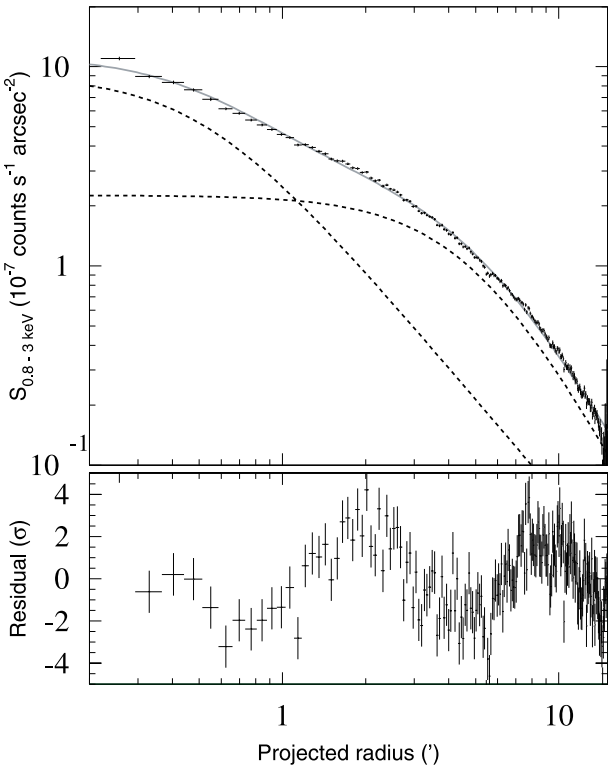


**Fig. 2.** In the upper panel, a radial profile of the surface brightness of AWM 7 in the 0.8–3 keV band is plotted for XMM-Newton MOS 1+2 ($r < 13'$). The best-fit double-$\beta$ model is shown by the solid gray line, and the two $\beta$-components are indicated by dashed lines. In the bottom panel, fit residuals are shown in units of $\sigma$, which correspond to the data minus the folded model, divided by the $1\,\sigma$ error of each data point.

**Table 3.** Best-fit parameters of figure 3.

| | $\beta$ | $r_{\rm c}$ | $S_{0.8-3\,\rm keV}$ * |
|---|---|---|---|
| narrower .... | $0.44 \pm 0.01$ | $0'.51 \pm 0'.02$ | $9.01 \pm 0.28$ |
| wider ..... | $0.60 \pm 0.01$ | $5'.06 \pm 0'.16$ | $2.26 \pm 0.08$ |

* $S_{0.8-3\,\rm keV}$ at the center in units of $10^{-7}$ counts s$^{-1}$ arcsec$^{-2}$.

## 3. Temperature and Abundance Profiles

### 3.1. Spectral Fit

We extracted spectra from seven annular regions of $0'$–$2'$, $2'$–$4'$, $4'$–$6'$, $6'$–$9'$, $9'$–$13'$, $13'$–$17'$, and $17'$–$27'$, centered on (RA, Dec) = ($2^{\rm h}54^{\rm m}32\overset{\rm s}{.}0$, $+41^\circ35'15''$). The inner four annuli were taken from the central observation, and the outer three annuli were from the two offset observations. Table 4 lists areas of the extraction regions (arcmin$^2$), the coverage of the whole annulus (%), the SOURCE_RATIO_REG values [2], and the observed counts in the range 0.4–8.1 keV including NXB and CXB for the BI and FI sensors.

The annular spectra are shown in figure 3. Emission lines from Mg, Si, S, Fe are clearly seen in the spectrum for each

[2] SOURCE_RATIO_REG represents flux ratio in the assumed spatial distribution on the sky (double-$\beta$ model) inside the accumulation region to the entire model, and written in the header keyword of the calculated ARF by "xissimarfgen".

Downloaded from https://academic.oup.com/pasj/article/60/sp1/S333/1461691 by guest on 16 August 2022

ring. Although the O VII and O VIII lines are prominent in the outer rings, most of the O VII emission is considered to come from the local Galactic emission.

The basic strategy for the spectral fit is described in subsection 4.2 of Sato et al. (2007a). The spectra for the east and west regions were fitted simultaneously according to the distance from the cluster center. The fit parameters were linked, except for normalization. We examine the difference between the east and west regions in subsection 3.4. The BI and FI spectra were also fitted simultaneously in the 0.4–8.1 keV band, excluding the response anomaly around the Si K-edge (1.825–1.840 keV). In a simultaneous fit, only the normalization was allowed to take different values between the BI and FI data, though the derived normalizations were quite consistent between the two.

### 3.2. Estimation of the Galactic Component

It is important to precisely estimate the foreground Galactic emission, for which the offset observations of AWM 7 give useful data. The Galactic component is prominent in the 17′–27′ annulus, as shown in figure 3; however, the ICM component is still dominant in almost the whole energy range, except for the O VII line. We also dealt with these data in the same way as in Sato et al. (2007a). We performed a simultaneous fit in the whole 0.4–8.1 keV range (except for 1.825–1.840 keV) for the spectra in 13′–17′ annulus of the west offset region and that in 17′–27′ annuli of the east and west offset regions. We assumed either a one or two temperature apec model for the Galactic component; the fit results are presented in table 5. The resultant normalizations of the apec models in table 5 were scaled so that they give the surface brightness per arcmin$^2$.

We examined the improvement of $\chi^2$ ($\Delta\chi^2 = 38$) values with the $F$-test; also, the addition of the apec$_2$ component was necessary with high significance (error probability $\sim 10^{-7}$). We further allowed normalization of the apec$_2$ to be free for those three annuli. We concluded that the two apec models are required to account for the Galactic component. Hereafter, the model apec$_1$ + apec$_2$ + phabs × vapec is used for the spectral fits, unless otherwise stated.

In order to take into account both the existence of the Galactic component, itself, and the propagation of its statistical error, we fitted the spectrum in each individual annulus simultaneously with that in the outermost annulus, i.e., at 17′–27′ in the east and west offset regions. The normalization for the sum of the apec$_1$ and apec$_2$ components was constrained to give the same surface brightness in all annuli, and the temperatures of these two apec models were also common for all of the regions including the 17′–27′ annuli. These common normalizations, $Norm_1$ and $Norm_2$, and the common temperatures, $kT_1$ and $kT_2$, were free parameters. The derived normalizations and temperatures for the Galactic components are consistent with the values already given in table 5b within their errors. The influence on the ICM temperature and the abundance due to modeling the Galactic component are examined in subsection 3.3.

### 3.3. Radial Temperature and Abundance Profiles

The fits are not acceptable mainly due to the very high photon statistics compared with systematic errors in the instrumental response. However, these results are useful to assess how effectively the metal abundances are constrained. We fitted the spectra with all of the metal abundances as free parameters. Somehow, the Ne and Ni abundances turn out to be higher than those of the other elements. This might be because the lines from these elements are not well resolved from the Fe-L line complex. We tentatively left these Ne and Ni abundances to vary freely in the spectral fit.

The resultant radial profiles of the temperature and the abundance are shown in figure 4. The temperature profile shows

**Table 4.** Properties for each annular region of AWM 7.

| Region* | Area† (arcmin$^2$) | Coverage†‡ | SOURCE_RATIO_REG$^2$ | Counts§ BI | FI |
|---|---|---|---|---|---|
| Center | | | | | |
| 0′–2′ | 12.6 | 100.0% | 12.0% | 21800 | 52737 |
| 2′–4′ | 37.7 | 100.0% | 19.1% | 38654 | 89901 |
| 4′–6′ | 62.8 | 100.0% | 15.8% | 33146 | 75797 |
| 6′–9′ | 136.1 | 96.3% | 15.2% | 34767 | 74968 |
| East | | | | | |
| 9′–13′ | 48.5 | 17.6% | 2.1% | 12755 | 26352 |
| 13′–17′ | 76.3 | 20.2% | 1.7% | 14577 | 31750 |
| 17′–27′ | 176.7 | 12.8% | 1.6% | 19242 | 39475 |
| West | | | | | |
| 9′–13′ | 46.3 | 16.7% | 2.1% | 10695 | 23108 |
| 13′–17′ | 72.7 | 19.3% | 1.6% | 11591 | 23745 |
| 17′–27′ | 182.9 | 13.2% | 1.7% | 16295 | 36026 |

* The inner four annuli are extracted from the central observation, and the outer annuli are from the east and west observations, respectively.
† The largest values among four sensors are presented.
‡ Coverage of the whole area.
§ Observed counts including NXB and CXB in 0.4–7.1 keV for BI and 0.4–8.1 keV for FI.

**Table 5.** Best-fit parameters of the apec component(s).*

| Fit model | $Norm_1$ † | $kT_1$ (keV) | $Norm_2$ † | $kT_2$ (keV) | $\chi^2$/dof |
|---|---|---|---|---|---|
| (a) apec$_1$ + phabs × vapec ..... | $7.52 \pm 0.70$ | $0.262^{+0.035}_{-0.013}$ | — | — | 1781/1495 |
| (b) apec$_1$ + apec$_2$ + phabs × vapec ..... | $6.59 \pm 0.46$ | $0.157^{+0.041}_{-0.035}$ | $0.32 \pm 0.07$ | $0.612^{+0.052}_{-0.055}$ | 1743/1493 |

* A simultaneous fit of the spectra in 13′–17′ and 17′–27′ annuli of the west offset region and in 17′–27′ annulus of the east offset region.
† Normalization of the apec component divided by the solid angle, $\Omega^{\rm U}$, assumed in the uniform-sky ARF calculation (20′ radius), $Norm = \int n_{\rm e} n_{\rm H} dV / [4\pi (1+z)^2 D_{\rm A}^2] / \Omega^{\rm U} \times 10^{-20}$ cm$^{-5}$ arcmin$^{-2}$, where $D_{\rm A}$ is the angular distance to the source.

Downloaded from https://academic.oup.com/pasj/article/60/sp1/S333/1461691 by guest on 16 August 2022

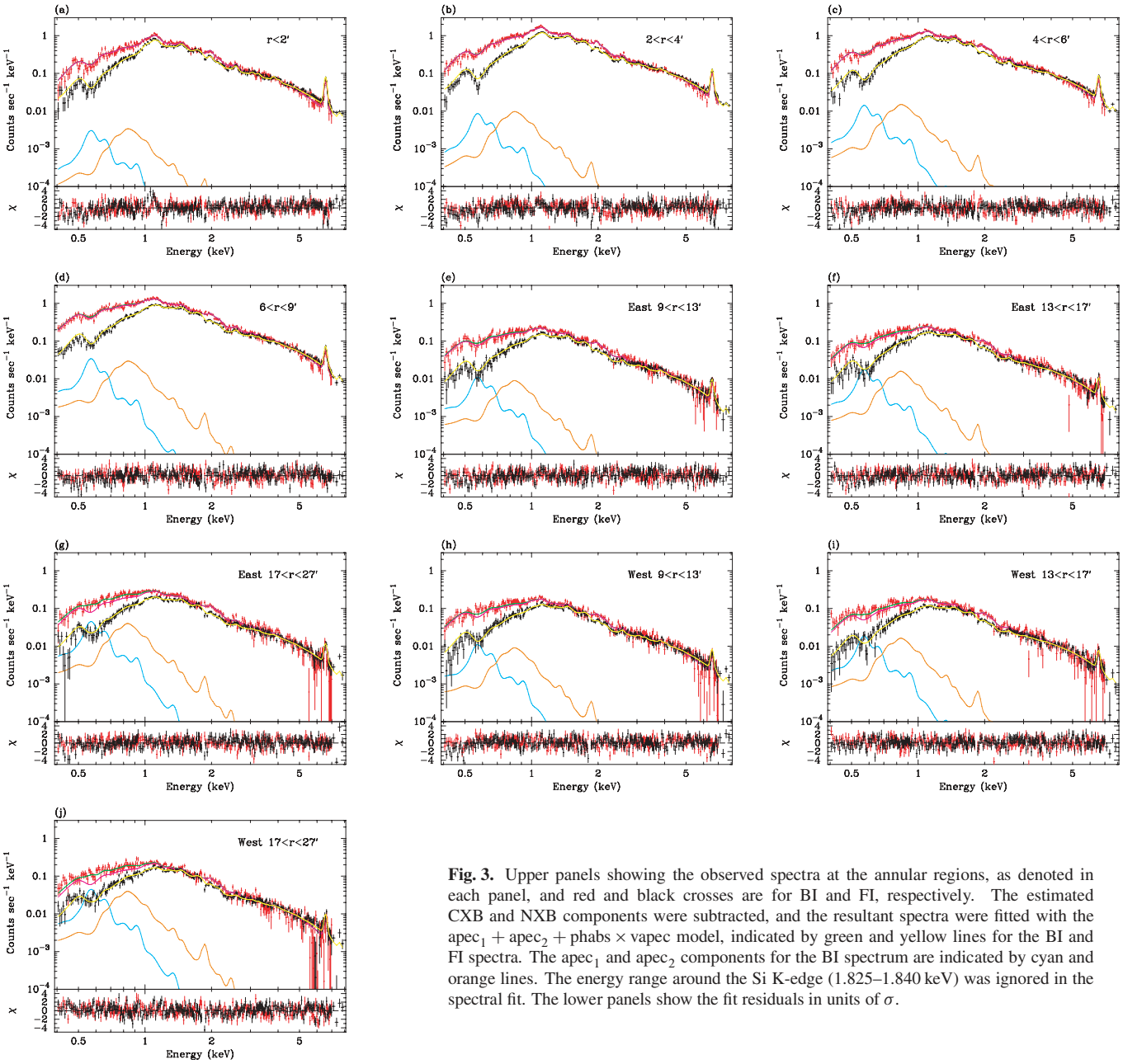


**Fig. 3.** Upper panels showing the observed spectra at the annular regions, as denoted in each panel, and red and black crosses are for BI and FI, respectively. The estimated CXB and NXB components were subtracted, and the resultant spectra were fitted with the $\mathrm{apec}_1 + \mathrm{apec}_2 + \mathrm{phabs} \times \mathrm{vapec}$ model, indicated by green and yellow lines for the BI and FI spectra. The $\mathrm{apec}_1$ and $\mathrm{apec}_2$ components for the BI spectrum are indicated by cyan and orange lines. The energy range around the Si K-edge (1.825–1.840 keV) was ignored in the spectral fit. The lower panels show the fit residuals in units of $\sigma$.

a mild cooling core in the central region ($r \lesssim 6'$), and declines from $\sim 3.8$ keV at the $6'$–$9'$ region ($\sim 130$ kpc) to $\sim 3.4$ keV in the outermost annulus of $17'$–$27'$ ($\sim 360$–$570$ kpc, $\sim 0.22$–$0.35\ r_{180}$). The abundance profiles of O, Mg, Si, S, and Fe were obtained up to a radius of $27' \simeq 570$ kpc. The abundances of Mg, Si, S, and Fe all decline with the radius from $\sim 1.5$, 1.1, 1.1, and 0.9 solar in the central region, to $\sim 0.9$, 0.4, 0.3, and 0.4 solar, respectively, in the cluster outskirts. The O abundance shows a somewhat flatter radial distribution.

Additional uncertainties on the derived parameters due to the OBF contaminant and the background (CXB + NXB) systematics are given in table 6 and figure 4. Here, we fitted the spectra again by changing the background normalization by $\pm 10\%$; the ranges of the parameters are plotted with light-gray dotted lines in figure 4. The systematic error in the background estimation is almost negligible. The change of the best-fit parameters by using alternative modeling of the Galactic component with a single-temperature apec model was investigated; the results are indicated with light-gray dash-dotted lines. The differences are within the statistical error for the inner-five annuli. However, O abundance becomes lower than the 90% confidence error range at the outer two annuli, and the temperature and Fe abundance become lower at the outermost annulus. This is due mainly to the fact that the XIS cannot resolve the ICM O VIII line from the Galactic one by the redshift. The systematic error range due to the uncertainty in the OBF contaminant is indicated by black dotted lines. A list of $\chi^2$/dof is presented in table 7.

Downloaded from https://academic.oup.com/pasj/article/60/sp1/S333/1461691 by guest on 16 August 2022

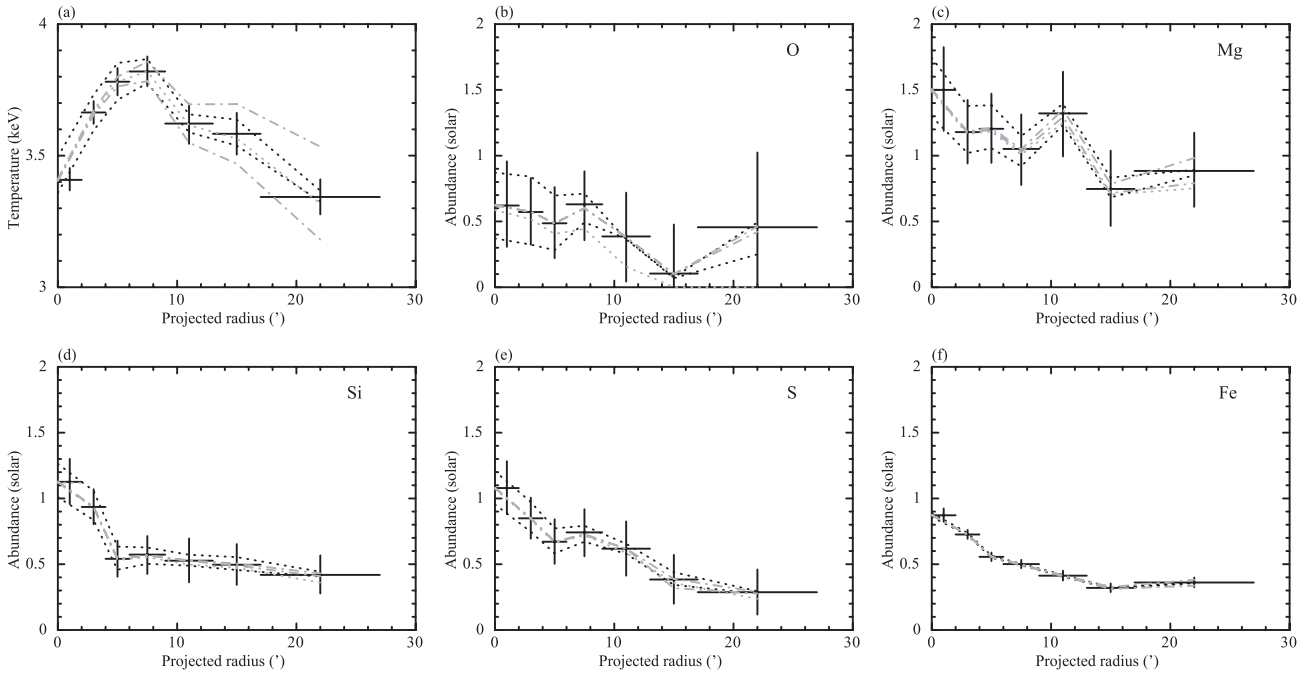


**Fig. 4.** (a) Radial temperature profiles derived from the spectral fit for each annulus. The horizontal axis denotes the projected radius. Black dotted lines indicate shifts of the best-fit values by changing the thickness of the OBF contaminant by $\pm 10\%$. Light-gray dotted lines denote those when the estimated CXB and NXB levels are changed by $\pm 10\%$. The light-gray dash-dotted line shows the best-fit value when the Galactic component is modeled by a single-temperature apec model. (b)–(f) Radial abundance profiles derived and plotted in the same way as in (a).

**Table 6.** Summary of the best-fit parameters of the vapec component for each annular region of AWM 7.*

| Region | *Norm*† | $kT$ (keV) | O (solar) | Ne (solar) | Mg (solar) | Si (solar) | S (solar) | Fe (solar) | Ni (solar) | $\chi^2$/dof |
|---|---|---|---|---|---|---|---|---|---|---|
| 0′–2′ | $1007 \pm 36$ | $3.41^{+0.04}_{-0.04}$ | $0.62^{+0.34}_{-0.31}$ | $2.11^{+0.40}_{-0.37}$ | $1.50^{+0.32}_{-0.31}$ | $1.13^{+0.18}_{-0.17}$ | $1.08^{+0.20}_{-0.20}$ | $0.87^{+0.05}_{-0.04}$ | $1.71^{+0.61}_{-0.58}$ | 1872/1493 |
| 2′–4′ | $595 \pm 16$ | $3.66^{+0.04}_{-0.04}$ | $0.57^{+0.26}_{-0.25}$ | $1.65^{+0.28}_{-0.27}$ | $1.18^{+0.24}_{-0.24}$ | $0.94^{+0.13}_{-0.13}$ | $0.85^{+0.16}_{-0.15}$ | $0.73^{+0.03}_{-0.03}$ | $1.47^{+0.47}_{-0.46}$ | 1899/1493 |
| 4′–6′ | $342 \pm 10$ | $3.78^{+0.05}_{-0.05}$ | $0.49^{+0.28}_{-0.26}$ | $1.38^{+0.29}_{-0.28}$ | $1.20^{+0.27}_{-0.27}$ | $0.54^{+0.14}_{-0.14}$ | $0.67^{+0.17}_{-0.17}$ | $0.56^{+0.03}_{-0.03}$ | $0.56^{+0.53}_{-0.52}$ | 1805/1493 |
| 6′–9′ | $182 \pm 5$ | $3.82^{+0.06}_{-0.06}$ | $0.63^{+0.25}_{-0.27}$ | $1.33^{+0.28}_{-0.29}$ | $1.05^{+0.26}_{-0.27}$ | $0.57^{+0.14}_{-0.15}$ | $0.74^{+0.18}_{-0.18}$ | $0.50^{+0.03}_{-0.03}$ | $2.11^{+0.57}_{-0.56}$ | 1816/1493 |
| 9′–13′ | $113 \pm 4$ | $3.62^{+0.08}_{-0.08}$ | $0.39^{+0.33}_{-0.34}$ | $1.08^{+0.33}_{-0.32}$ | $1.32^{+0.32}_{-0.33}$ | $0.53^{+0.17}_{-0.17}$ | $0.62^{+0.21}_{-0.21}$ | $0.41^{+0.04}_{-0.04}$ | $2.33^{+0.70}_{-0.68}$ | 2361/2014 |
| 13′–17′ | $72 \pm 2$ | $3.58^{+0.08}_{-0.08}$ | $0.10^{+0.37}_{-0.10}$ | $0.86^{+0.30}_{-0.31}$ | $0.75^{+0.29}_{-0.28}$ | $0.50^{+0.16}_{-0.15}$ | $0.38^{+0.19}_{-0.18}$ | $0.32^{+0.03}_{-0.03}$ | $1.22^{+0.64}_{-0.61}$ | 2370/2014 |
| 17′–27′‡ | $29 \pm 1$ | $3.34^{+0.07}_{-0.07}$ | $0.46^{+0.57}_{-0.46}$ | $0.91^{+0.32}_{-0.31}$ | $0.88^{+0.29}_{-0.27}$ | $0.42^{+0.15}_{-0.14}$ | $0.29^{+0.17}_{-0.17}$ | $0.36^{+0.04}_{-0.04}$ | $1.88^{+0.64}_{-0.60}$ | —‡ |

* Fit with the $\mathrm{apec}_1 + \mathrm{apec}_2 + \mathrm{phabs} \times \mathrm{vapec}$ model. The spectrum in each annulus was simultaneously fitted with the outermost 17′–27′ spectrum obtained by two offset observations. The errors show a 90% confidence statistical error range, without including systematic errors. These results are shown in figure 4, where the Ne and Ni abundances may have large systematic uncertainties, because XIS cannot resolve the ionized Ne lines from the Fe-L line complex.

† Normalization of the vapec component scaled with a factor of SOURCE_RATIO_REG / AREA in table 4, $Norm = \frac{\mathrm{SOURCE\_RATIO\_REG}}{\mathrm{AREA}} \int n_\mathrm{e} n_\mathrm{H} dV / [4\pi (1+z)^2 D_\mathrm{A}^2] \times 10^{-20}$ cm$^{-5}$ arcmin$^{-2}$, where $D_\mathrm{A}$ is the angular distance to the source. For the offset regions, these are the values of normalization of the east region.

‡ The 17′–27′ annulus of the east and west offset regions were fitted simultaneously with other annuli, and the best-fit values with the 13′–17′ annulus of the east and west offset regions, respectively, are presented here.

### *3.4. Difference between East and West Regions*

We examined the difference in the temperature and abundance profiles between the east and west directions from the cluster center. We treated the spectra in the east and west regions separately, but they were always fitted jointly with the outermost spectrum in 17′–27′ where the east and west data were combined together in the same way as described in subsection 3.2. Figure 5a shows the temperature profile along the east–west direction of the cluster. The west direction shows a slightly steeper temperature gradient than the east direction. Figures 5b–5d also show the abundance ratios of O, Mg, and Si divided by Fe, in order to look into the relative variation in the abundance profiles. While the Si/Fe ratio is consistent to be constant along the east–west direction, the Mg/Fe ratio

Downloaded from https://academic.oup.com/pasj/article/60/sp1/S333/1461691 by guest on 16 August 2022

**Table 7.** List of $\chi^2$/dof for each fit of AWM 7.

| Region | Nominal | Contaminant | | Background | |
|---|---|---|---|---|---|
| | | +10% | −10% | +10% | −10% |
| Center ..... | | | | | |
| 0′–2′ ..... | 1872/1493 | 1829/1493 | 1939/1493 | 1909/1493 | 1871/1493 |
| 2′–4′ ..... | 1899/1493 | 1876/1493 | 1965/1493 | 1937/1493 | 1897/1493 |
| 4′–6′ ..... | 1805/1493 | 1789/1493 | 1849/1493 | 1844/1493 | 1803/1493 |
| 6′–9′ ..... | 1816/1493 | 1786/1493 | 1852/1493 | 1858/1493 | 1814/1493 |
| East and West | | | | | |
| 9′–13′ ..... | 2361/2014 | 2337/2014 | 2395/2014 | 2408/2014 | 2355/2014 |
| 13′–17′ ..... | 2370/2014 | 2365/2014 | 2390/2014 | 2424/2014 | 2362/2014 |

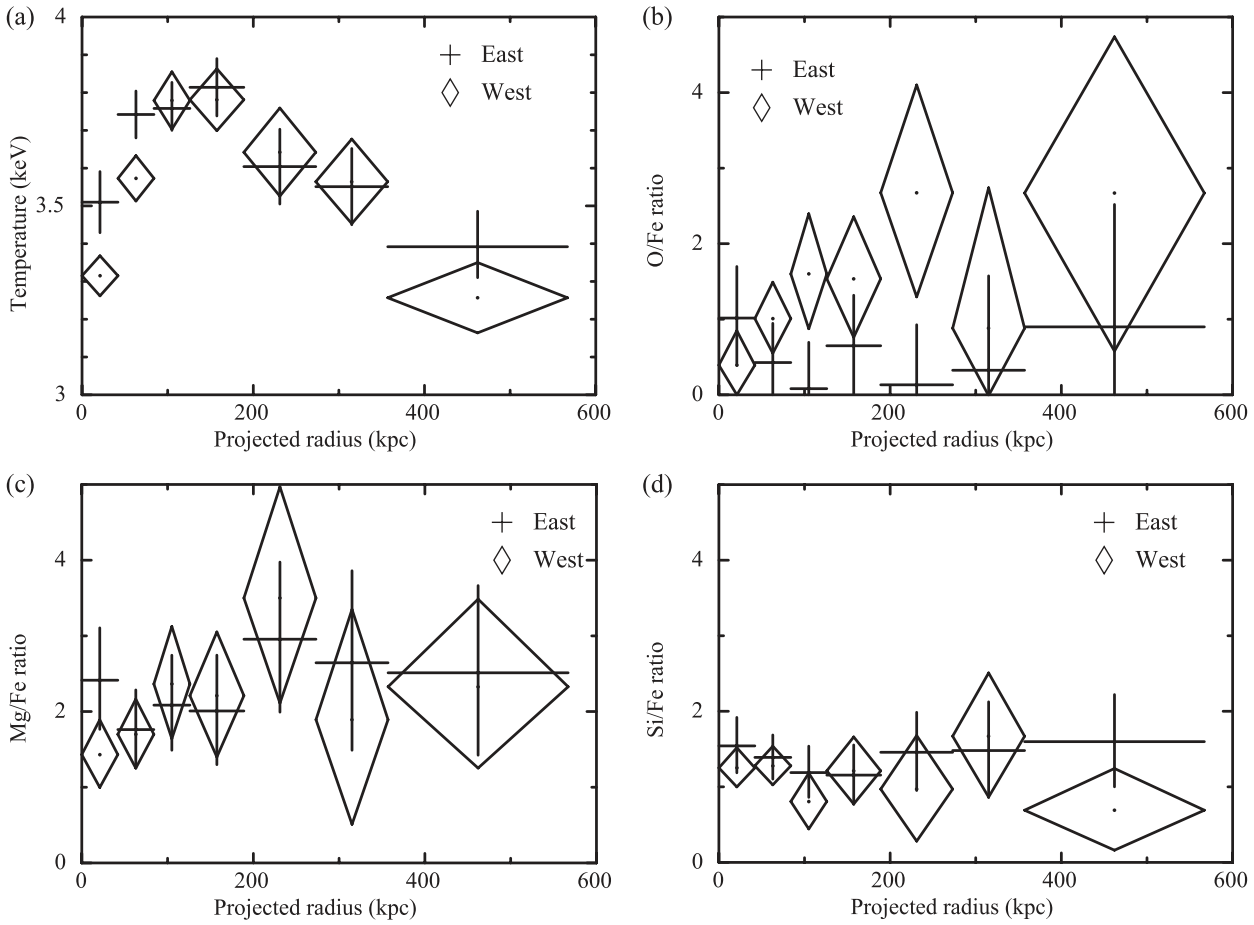


**Fig. 5.** (a) Radial temperature profile along the east–west direction. (b)–(d) Radial O, Mg, and Si to Fe abundance ratios along with the east and west directions, same as (a).

appears to show an increase with the radius in both directions. Although the O/Fe ratio has a large uncertainty, the west direction shows lager values than the east.

## 4. Bulk Motions in the ICM

### *4.1. Spectral Analysis in Search of Bulk Motions*

In order to search for possible bulk motions of the ICM, the central energy of He-like Fe-K line (the rest-frame energy of 6.679 keV) was examined in order to look into a positional variation. We divided the $18' \times 18'$ square XIS field of view into smaller cells. The central observation was divided into 16-times $2.'2 \times 2.'2$ cells, 12-times $4.'5 \times 4.'5$ cells as shown in figure 6a. For the east and west offset regions, we divided each field into 6-times $4.'5 \times 8.'9$, 3-times $8.'9 \times 8.'9$, and one $17.'8 \times 8.'9$ cells. We co-added the data from only the FI sensors (XIS 0, 2, and 3). For an accurate determination of the iron-line energy, we fitted the background-subtracted XIS (FI) spectra

Downloaded from https://academic.oup.com/pasj/article/60/sp1/S333/1461691 by guest on 16 August 2022

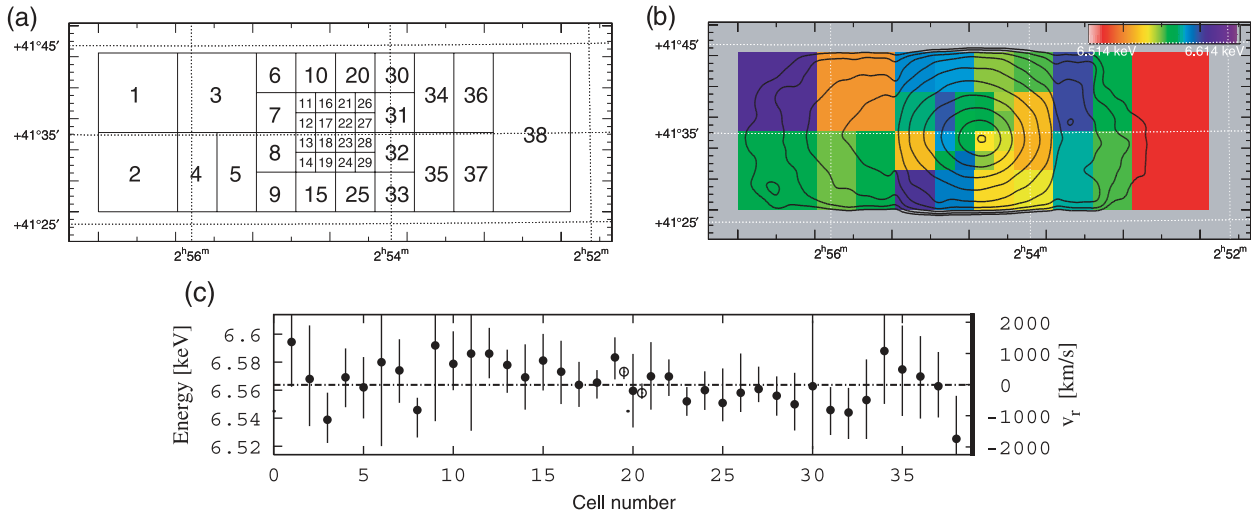


**Fig. 6.** Measurement of the bulk motion using the central energy of the He-like Fe-K lines. (a) Spatial division and the position numbers. Depending of the brightness, the whole observed region is divided into $2\farcm2 \times 2\farcm2$ (16 cells) or $4\farcm5 \times 4\farcm5$ (12 cells) regions for the central observation, and into $4\farcm5 \times 8\farcm9$ (6 cells), $8\farcm9 \times 8\farcm9$ (3 cells), and $17\farcm8 \times 8\farcm9$ (1 cell) regions for the offset observations. (b) Color representation of the spatial distribution of the central energy of redshifted iron line for each cell. The map is overlaid on the contour in figure 1. (c) Energy of the He-like Fe-K line against the cell numbers. The energy of redshifted He-like Fe-K$\alpha$ line at AWM 7 ($z = 0.01724$) is 6.566 keV. The dot-dashed line corresponds to the cluster redshift, and the dotted lines indicate the calibration error range ($z = 0.003$ or $\sim 20$ eV) of XIS. Open circles indicate the average for the east or west region in the central pointing.

with a simple model over the 5–10 keV energy range. The model used consisted of a continuum represented by a power-law model and Gaussian profiles as described in Ota et al. (2007); we determined the central energy of the He-like Fe-K$\alpha$ line. In the fit, we fixed the intrinsic width of the Gaussian line to be 0. We employed the central energies of He-like Fe-K$\alpha$ and H-like Fe-K$\alpha$ lines at the rest frame to be 6.679 and 6.964 keV, respectively, which are expected from an apec model with $kT = 3.5$ keV.

### 4.2. *Constraint on the Existence of Bulk Motions*

The distribution of the line central energy is shown as a color-coded map in figure 6b and against the cell number in figure 6c, with 90% confidence statistical errors. The dot-dashed line in figure 6c corresponds to the redshifted central energy at AWM 7 of $E_{\rm cl} = 6.566$ keV with $z = 0.01724$, based on the rest-frame central energy, $E_0 = 6.679$ keV. The dotted lines show the range of the current calibration error of $z = 0.003$ or $\sim 20$ eV. Figures 6b and 6c indicate no significant systematic feature for the gas motion within the 90% confidence level.

Since there seem to be some hint of a difference between the east and west regions in the central observation, we looked into a larger structure. The spectra in the cell numbers of 6–19, or 20–33 were summed up to evaluate the east or west difference for the central pointing, respectively. The results for the east and west regions correspond to the left and right open circles in figure 6c. The difference was $15 \pm 6$ eV between the east and west regions with the 90% confidence error. However, it is known that the central energy of a line shows a dependence on the read-out direction of the XIS chip, and the systematic uncertainty is about $\sim 20$ eV. We therefore conclude the upper limit for the bulk motion of the gas to be $\Delta E \lesssim 40$ $(15 \pm 6 \pm 20)$ eV, based on a measurement of the central energy of the He-like Fe-K$\alpha$ line, which corresponds to $\Delta v \lesssim 2000$ km s$^{-1}$.

## 5. Discussion

### 5.1. *Temperature Profile*

Suzaku observations showed the temperature profile of AWM 7 to about the $\sim 0.35 r_{180}$ region of the cluster, extending the previous Chandra and XMM-Newton measurements. Hayakawa (2006) showed the temperature in AWM 7 to drop from 3.8 keV at the peak to 3.5 keV at $r \sim 13'$ with XMM-Newton; the present study confirmed their results over a wider range of radius. Although previous ASCA observations of AWM 7 indicated a fairly uniform temperature distribution in the whole cluster region (Furusho et al. 2001; Ezawa et al. 1997), their results are consistent with ours within the error, because the temperature drop is so small that it could well be regarded as being isothermal in observations with lower statistics.

To compare the temperature profile with those in other clusters, we normalized the temperature with the emission-weighted average of $k\langle T \rangle = 3.56$ keV for AWM 7, and plotted it against the radius normalized with the virial radius in figure 7. We calculated the $k\langle T \rangle$ in the range of 0.1–0.3 $r_{180}$ with Suzaku. The normalized temperature profile was compared with Abell 1060, which shows $k\langle T \rangle = 2.49$ keV in 0.1–0.25 $r_{180}$ (Sato et al. 2007a). Note that AWM 7 has a cD galaxy at the center, while Abell 1060 does not. The temperature gradient of AWM 7 is clearly less steep than that of Abell 1060, while these profiles are both consistent with the broad range (dashed line region in figure 7) given by Markevitch et al. (1998) with ASCA. The Markevitch et al. (1998) result is consistent with the temperature gradients for several clusters studied by Vikhlinin et al. (2005) with Chandra

Downloaded from https://academic.oup.com/pasj/article/60/sp1/S333/1461691 by guest on 16 August 2022

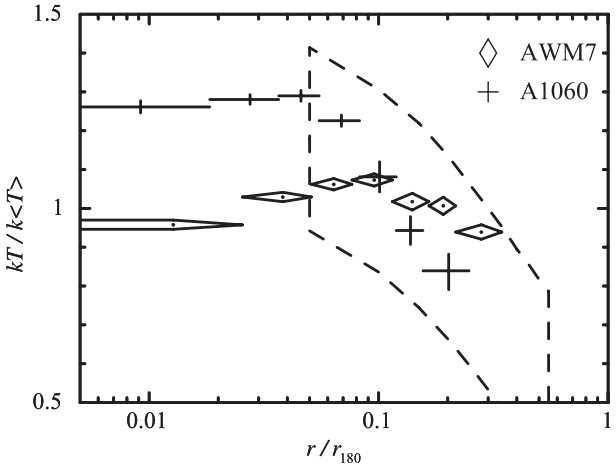


**Fig. 7.** Scaled temperature profiles using normalized temperatures and the radius scaled by the virial radius. The Abell 1060 data are taken from Sato et al. (2007a). The region indicated by dashed line shows result of ASCA observations by Markevitch et al. (1998).

and Piffaretti et al. (2005) with XMM-Newton.

Hayakawa (2006) showed a systematic difference with XMM-Newton in the temperature gradients between 9 cD and 13 non-cD clusters, including both AWM 7 and Abell 1060. They showed that both cD and non-cD clusters have consistent gradients for a radius range of $0.05 < r/r_{180} < 0.55$, in general agreement with the Markevitch et al. (1998) result, with slightly higher absolute temperatures. They, however, found that, in $r/r_{180} < 0.05$, the temperatures of the cD clusters showed a systematic drop toward the center, and this feature was not clearly recognized in the non-cD clusters. Such a feature in the central region is also seen in our observations of AWM 7.

### 5.2. *Abundance Profiles*

The good XIS sensitivity to emission lines, especially below 1 keV, enabled us to measure the O and Mg abundances out to $\sim 0.35\ r_{180}$ with Suzaku. The radial abundance profiles of Si, S, and Fe show steeper drops than those of O and Mg. Ezawa et al. (1997) reported a large-scale abundance gradient from 0.5 solar at the center to $\lesssim 0.2$ solar in the region over 500 kpc ($H_0 = 50\,\mathrm{km\,s^{-1}\,Mpc^{-1}}$), consistent with our result for Fe. On the other hand, the abundance determinations of Ni and Ne have a problem because of possible confusion with strong Fe-L lines. Also, we have to note that the O abundance in the outer region of our observations is strongly affected by the foreground Galactic emission, as described in subsection 3.2. Even allowing the O distribution to be a rather preliminary result, the combined Mg and O feature suggests that their distribution is likely to be more extended than those of Fe and Si. This is at least consistent with the view that the metals injected from type II supernovae (SNe II), i.e., O and Mg, in the early phase of galaxy formation in the wind form, show an extended distribution (Arimoto & Yoshii 1987). In contrast, the steep gradient of the Fe and Si distributions suggests they are mostly produced by type Ia supernovae (SNe Ia) at a later stage, with an enhanced contribution from the cD galaxy, as shown by De Grandi et al. (2004).

We calculated cumulative metal mass profiles by combining the present abundance results with the X-ray gas mass profile observed with XMM-Newton. Since the measured metals have different yields from the two types of supernova, with O and Mg mostly synthesized by SNe II, while SNe Ia give large yields of Si, S, and Fe, we can estimate their relative contributions that can best account for the measured abundance pattern. We thus estimated the number ratio of SNe II to SNe Ia to be $\sim 4$ in the ICM of AWM 7, as reported in Sato et al. (2007b). We also calculated the radial mass-to-light ratios for O, Mg, and Fe, and compared the values with those in other systems. As a result, it is suggested that smaller systems with lower gas temperature tend to show lower mass-to-light ratios for O, Mg, and Fe as shown in K. Sato et al. (2008, in preparation).

### 5.3. *Morphology of AWM 7*

No significant bulk motion of the gas exceeding the sound speed, $\sim 1000\,\mathrm{km\,s^{-1}}$, was detected in the ICM of AWM 7, even though the X-ray image of AWM 7 is highly elongated in the east–west direction. Neumann and Böhringer (1995) and Furusho et al. (2001) reported the major-to-minor axis ratio to be 0.8. This elongation is fairly parallel to the large-scale filament of the Pisces–Perseus supercluster, which runs almost along the east–west direction. We consider possible processes to explain this elongation. In general, the simplest explanation for the deviation from the spherical symmetric shape is that the cluster is rotating. However, X-ray spectra presently show no indication of significant rotation. Furthermore, based on the standard CDM scenario, it is difficult to make a cluster to have a large angular momentum (e.g. Peebles 1969; White 1984; Barnes & Efstathiou 1987). Tidal interaction with the Perseus cluster is another possible process; however, Neumann and Böhringer (1995) showed that the tidal effect of the Perseus cluster was too small to cause the observed large ellipticity of AWM 7.

Another possible process is an asymmetric accretion of matter (see e.g., Neumann & Böhringer 1995). Directional mass accretion may lead to an ellipsoidal or triaxial dark-matter halo. If the intracluster gas is in hydrostatic equilibrium in the gravitational potential dominated by the dark matter, the gas distribution should deviate from spherical symmetry. If we can obtain more-detailed information about the profile of the eccentricity of the gas isodensity surface, as well as precise density and temperature profiles, we can reconstruct the three-dimensional dark-matter structure (e.g., Lee & Suto 2004). This will give us an important information about the dark matter relaxation process.

Finally, if the gas infalls in an asymmetric manner from the filament onto the relaxed cluster, and the accreted gas has not been mixed with the original intracluster gas, the gas profile deviates from spherical symmetry, and the X-ray morphology becomes elliptical. In this case, the gas in the outer part of the east and west regions may keep the physical properties, such as the metal abundance when the gas was in the filament. The warm gas in the large-scale filament is an important part of the warm–hot intergalactic medium (WHIM), which is the dominant component of baryons in the local universe (e.g., Yoshikawa et al. 2003). Several missions are proposed to detect WHIM through O VII and

Downloaded from https://academic.oup.com/pasj/article/60/sp1/S333/1461691 by guest on 16 August 2022

O VIII emission lines (e.g., Ishisaki et al. 2004; Ohashi et al. 2006; Piro et al. 2006; den Herder et al. 2006). If the metal abundance of gas in filaments is as high as that of the ICM, the detection of WHIM becomes relatively easy, and the missing baryon problem can be answered in the near future. Furthermore, we need to revisit the metal production and ejection processes closely to explain the high metal abundance in the intergalactic gas. To confirm such a possibility, deeper X-ray observations in the outermost region of AWM 7 are important.

Part of this work was financially supported by the Ministry of Education, Culture, Sports, Science and Technology, Grant-in-Aid for Scientific Research Nos. 14079103, 15340088, 15001002, 16340077, 18740011, 19840043.

## References

Anders, E., & Grevesse, N. 1989, Geochim. Cosmochim. Acta, 53, 197
Arimoto, N., & Yoshii, Y. 1987, A&A, 173, 23
Barnes, J., & Efstathiou, G. 1987, ApJ, 319, 575
De Grandi, S., Ettori, S., Longhetti, M., & Molendi, S. 2004, A&A, 419, 7
den Herder, J.-W., et al. 2006, Proc. SPIE, 62660H
Dickey, J. M., & Lockman, F. J. 1990, ARA&A, 28, 215
Dupke, R. A., & Bregman, J. N. 2001, ApJ, 562, 266
Dupke, R. A., & Bregman, J. N. 2006, ApJ, 639, 781
Ezawa, H., Fukazawa, Y., Makishima, K., Ohashi, T., Takahara, F., Xu, H., & Yamasaki, N. Y. 1997, ApJ, 490, L33
Finoguenov, A., Matsushita, K., Böhringer, H., Ikebe, Y., & Arnaud, M. 2002, A&A, 381, 21
Fukazawa, Y., Kawano, N., & Kawashima, K. 2004, ApJ, 606, L109
Furusho, T., Yamasaki, N. Y., & Ohashi, T. 2003, ApJ, 596, 181
Furusho, T., Yamasaki, N. Y., Ohashi, T. S. R., Kagei, T., Ishisaki, Y., Kikuchi, K., Ezawa, H., & Ikebe, Y. 2001, PASJ, 53, 421
Hayakawa, A. 2006, PhD thesis, Tokyo Metropolitan University
Hayakawa, A., Hoshino, A., Ishida, M., Furusho, T., Yamasaki, N. Y., & Ohashi, T. 2006, PASJ, 58, 695
Ishisaki, Y., et al. 2004, Proc. SPIE, 5501, 123
Ishisaki, Y., et al. 2007, PASJ, 59, S113
Koyama, K., et al. 2007, PASJ, 59, S23
Kushino, A., Ishisaki, Y., Morita, U., Yamasaki, N. Y., Ishida, M., Ohashi, T., & Ueda, Y. 2002, PASJ, 54, 327
Lee, J., & Suto, Y. 2004, ApJ, 601, 599
Markevitch, M., Forman, W. R., Sarazin, C. L., & Vikhlinin, A. 1998, ApJ, 503, 77
Matsushita, K., Böhringer, H., Takahashi, I., & Ikebe, Y. 2007, A&A, 462, 953
Matsushita, K., Finoguenov, A., & Böhringer, H. 2003, A&A, 401, 443
Mitsuda, K., et al. 2007, PASJ, 59, S1
Neumann, D. M., & Böhringer, H. 1995, A&A, 301, 865
Ohashi, T., et al. 2006, Proc. SPIE, 62660G,
Ota, N., et al. 2007, PASJ, 59, S351
Peebles, P. J. E. 1969, ApJ, 155, 393
Piffaretti, R., Jetzer, P., Kaastra, J. S., & Tamura, T. 2005, A&A, 433, 101
Piro, L., et al. 2006, Proc. SPIE, 62660K,
Read, A. M., & Ponman, T. J. 2003, A&A, 409, 395
Sato, K., et al. 2007a, PASJ, 59, 299
Sato, K., Tokoi, K., Matsushita, K., Ishisaki, Y., Yamasaki, N. Y., Ishida, M., & Ohashi, T. 2007b, ApJ, 667, L41
Tamura, T., Kaastra, J. S., den Herder, J. W. A., Bleeker, J. A. M., & Peterson, J. R. 2004, A&A, 420, 135
Vikhlinin, A., Markevitch, M., Murray, S. S., Jones, C., Forman, W., & Van Speybroeck, L. 2005, ApJ, 628, 655
White, D. A. 2000, MNRAS, 312, 663
White, S. D. M. 1984, ApJ, 286, 38
Yoshikawa, K., Yamasaki, N. Y., Suto, Y., Ohashi, T., Mitsuda, K., Tawara, Y., & Furuzawa, A. 2003, PASJ, 55, 879

Downloaded from https://academic.oup.com/pasj/article/60/sp1/S333/1461691 by guest on 16 August 2022